

The Mean and Turbulent Properties of a Wildfire Convective Plume

NEIL P. LAREAU AND CRAIG B. CLEMENTS

*Fire Weather Research Laboratory, Department of Meteorology and Climate Science,
San José State University, San Jose, California*

(Manuscript received 28 November 2016, in final form 14 June 2017)

ABSTRACT

The time-mean and time-varying smoke and velocity structure of a wildfire convective plume is examined using a high-resolution scanning Doppler lidar. The mean plume is shown to exhibit the archetypal form of a bent-over plume in a crosswind, matching the well-established Briggs plume-rise equation. The plume cross section is approximately Gaussian and the plume radius increases linearly with height, consistent with plume-rise theory. The Briggs plume-rise equation is subsequently inverted to estimate the mean fire-generated sensible heat flux, which is found to be 87 kW m^{-2} . The mean radial velocity structure of the plume indicates flow convergence into the plume base and regions of both convective overshoot and sinking flow in the upper plume. The updraft speed in the lower plume is estimated to be 13.5 m s^{-1} by tracking the leading edge of a convective element ascending through the plume. The lidar data also reveal aspects of entrainment processes during the plume rise. For example, the covariation of the radial velocity and smoke perturbations are shown to dilute the smoke concentration with height.


1. Introduction

Smoke dispersion is strongly affected by the structure and evolution of wildfire convective plumes. When wildfire plumes penetrate into the free troposphere they inject smoke aloft, causing regional- to global-scale impacts such as reduced insolation (Penner et al. 1992) and modified cloud microphysics (Andreae et al. 2004). On the other hand, when plumes remain confined within the atmospheric boundary layer, the smoke can more directly impact human populations, posing serious health hazards for affected communities (Delfino et al. 2009; Wegesser et al. 2009; Holstius et al. 2012; Johnston et al. 2012). Near-surface smoke can also cause persistent temperature inversions (Robock 1988, 1991), unexpected patterns of smoke transport (Lareau and Clements 2015), and travel hazards due to reduced visibility (Ashley et al. 2015). Satellite observations indicate that only a small fraction (4%–12%) of smoke plumes extend above the boundary layer (Kahn et al. 2008; Val Martin et al. 2010), but detailed observations

of the plume-rise dynamics leading to variations in smoke injection height are lacking.

To date, most of our knowledge of convective plume-rise dynamics stems from laboratory tank experiments and theory. From experiments, simple formulas for plume rise in neutral and continuous stratification have been developed (Morton et al. 1956; Scorer 1957). Semiempirical formulas have also been established for more-complex cases with crosswinds and density-stratified interfaces (Richards 1961, 1963; Saunders 1962; Linden 1973; Briggs 1975; Manins 1979). Among these formulations, Briggs's equation for buoyant plumes in a crosswind has gained widespread use and has been validated for a range of heat fluxes from industrial sources (Briggs 1975; Weil 1988). Benech et al. (1988), for example, found good agreement between observations of plume rise during the "Météotron" oil-burner experiments (Benech 1976; Church et al. 1980) and the Briggs equation.

The applicability of the Briggs plume-rise equation for wildfire plumes is, however, less clear. Raffuse et al. (2012) found systematic underprediction of smoke injection depth using the Briggs equation (embedded in a weather model) as compared with satellite lidar measurements. On the other hand, Cunningham and Goodrick (2013) found relatively good agreement between plume rise in a large-eddy simulation and the Briggs equation, at

 Denotes content that is immediately available upon publication as open access.

Corresponding author: Neil P. Lareau, neil.lareau@sjsu.edu

least in terms of plume centerline for an isolated plume. Plume isolation, however, is not necessarily observed during fires, and [Achtmeier et al. \(2011\)](#) attributed some of the disparities between observed smoke dispersion from a prescribed fire and the Briggs plume-rise predictions to the occurrence of multicore updrafts. More dynamically complete models than the Briggs empirical plume-rise equation may better predict plume behavior from such plumes ([Achtmeier et al. 2011](#)), and prognostic plume-rise equations that are based on the governing physics are now increasingly used to predict wildfire smoke injection heights ([Freitas et al. 2006, 2007, 2010](#); [Val Martin et al. 2012](#)).

Underlying some of the uncertainty in applying plume-rise predictions to wildfires is the general sparsity of high-spatial- and high-temporal-resolution observations of plume-rise dynamics. A notable exception is [Banta et al. \(1992\)](#), wherein lidar and radar observations of smoke columns indicated time-varying plume geometry, counterrotating vortex pairs, whole-column rotation, convergent near-surface flow, and pyroconvective clouds. None of these processes are explicitly represented in current plume-rise predictions. [Charland and Clements \(2013\)](#) also used Doppler lidar to examine the kinematics of a small grass-fire plume, finding strong radial convergence downwind of the plume base. [Lareau and Clements \(2016\)](#) more recently showed lidar and radar observations of pyrocumulonimbus (pyroCb) initiation from wildfire plumes. The onset of pyroCb can complicate the plume-rise dynamics because of the release of latent heat in the upper portions of the smoke column ([Trentmann et al. 2006](#); [Luderer et al. 2006, 2009](#); [Freitas et al. 2007](#); [Fromm et al. 2010](#)).

The goal of this study is to add to the observational basis for assessing wildfire plume-rise predictions in the lower troposphere. To be specific, we contribute new high-resolution observations of plume rise during a wildfire in Yosemite National Park in California. Using scanning Doppler lidar and other instruments, we examine the time-mean and time-varying properties of an isolated convective plume that developed from an expanding flank of the fire. From these data we test the applicability of the Briggs equation for describing the observed plume-rise properties. We also examine some of the entrainment processes that dilute the plume with height and thus affect the plume rise.

2. Data and methods

The plume observations were obtained using a pickup truck equipped with a scanning Doppler lidar, microwave profiler, radiosonde system, and an automated weather station ([Clements and Oliphant 2014](#)). The

key instrument in this study is the scanning Doppler lidar, which emits a $1.5\text{-}\mu\text{m}$ laser beam and records two range-resolved quantities: 1) the attenuated backscatter coefficient ($\text{m}^{-1}\text{sr}^{-1}$), which is a range-corrected measure of backscattered energy, and 2) the Doppler velocity (m s^{-1}). The lidar has a range-gate resolution of 18 m and a total range of 9.6 km. The Doppler velocity range is $\pm 19\text{ m s}^{-1}$, with an accuracy of $3\text{--}4\text{ cm s}^{-1}$ ([Pearson et al. 2009](#)).

The lidar-attenuated backscatter coefficient (hereinafter backscatter) is sensitive to micrometer-sized aerosol, including smoke. Smoke typically exhibits a lognormal size distribution with a peak near $0.13\text{ }\mu\text{m}$ but with a long tail extending toward coarser particles ([Radke et al. 1990, 1991](#); [Banta et al. 1992](#); [Reid and Hobbs 1998](#); [Reid et al. 2005](#)). For intense forest fires, supergiant aerosol particles are also typically present, with sizes up to and exceeding 1 mm. Using a radiative transfer model, [Banta et al. \(1992\)](#) showed that the lidar backscatter due to the numerous small smoke particles is comparable to the backscatter from the sparser large particles and that the logarithm of the backscatter is roughly proportional to the smoke concentration. Because of this sensitivity, near-IR lidars have been used to study smoke plumes and dispersion processes in numerous studies ([Benech et al. 1988](#); [Banta et al. 1992](#); [Kovalev et al. 2005](#); [Hiscox et al. 2006](#); [Charland and Clements 2013](#); [Clements et al. 2016](#); [Lareau and Clements 2015, 2016](#)).

In this study, the lidar was used to conduct range–height indicator (RHI) scans centered on the upright portion of a wildfire convective plume. Early in the plume evolution the RHI scans spanned from -5° to 70° in elevation angle, with some later scans extended to 130° . The average elevation step between data points is 0.73° , yielding a spatial resolution of $\sim 31\text{ m}$ between elevation steps at the range of the plume base (2500 m). Most RHIs were completed in 44–45 s. The lidar data were postprocessed by interpolation to a common polar coordinate grid, which facilitates computing mean and variance statistics. All backscatter data are presented as the base-10 logarithm of the recorded values.

Other ancillary data used in this study include observations from a GRAW Radiosondes GmbH GS-E radiosonde system, a Radiometrics Corporation MP-3000A microwave profiler, and remote automated weather stations within 25 km of the fire. The weather station data are obtained from MesoWest ([Horel et al. 2002](#)).

3. The El Portal fire

The El Portal fire started on 26 July 2014 near the entrance to Yosemite National Park ([Fig. 1a](#)). The

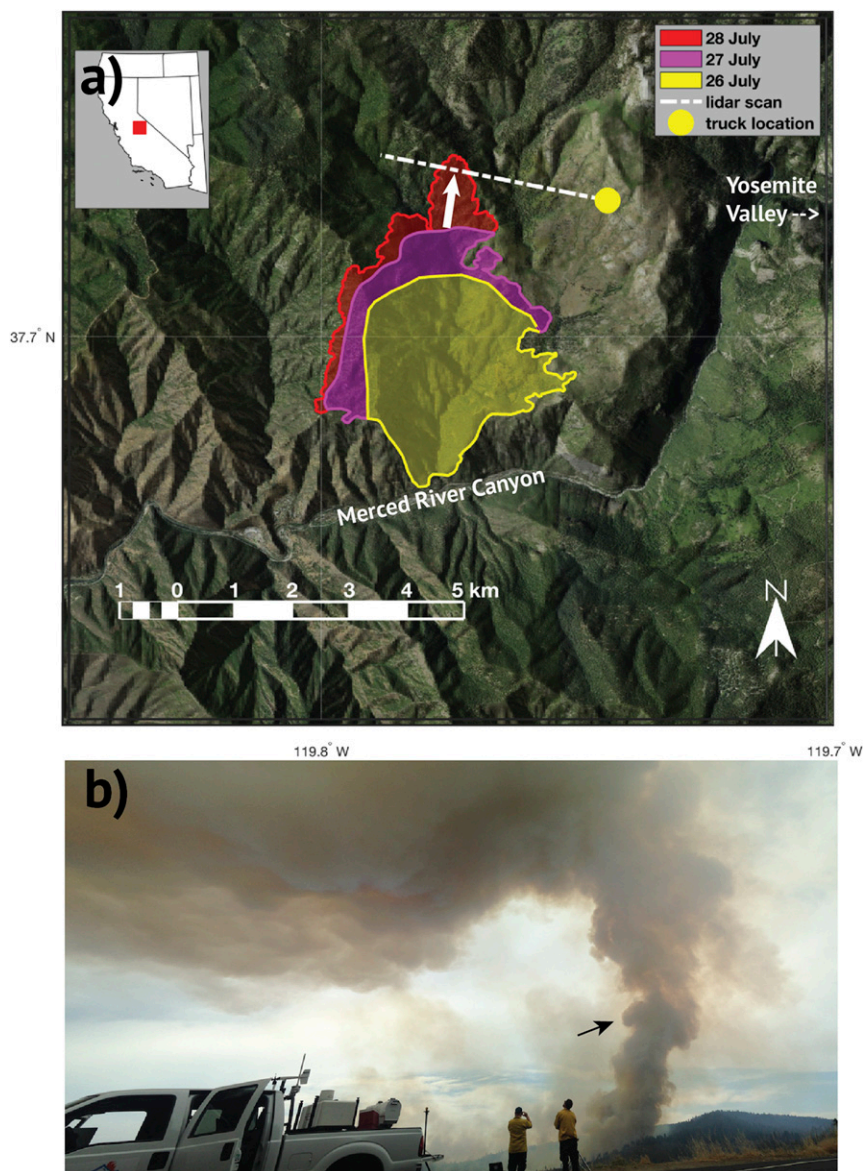


FIG. 1. Overview of the El Portal fire. (a) Fire perimeters for 26–28 Jul (transparent color fill) and the local topography (hill-shaded satellite image). The fire’s growth pattern leading to the observed plume is shown with a white arrow. The scan path of the lidar is shown as a dashed white line. (b) A photograph of the smoke plume at 1502 PDT showing the truck-mounted instruments and the structure of the convective column. The view is approximately along the dashed white line in (a) such that the photograph is looking to the west-northwest (i.e., $\sim 277^\circ$). The black arrow indicates one of many plume edge vortices that were observed.

initial growth was rapid (777 ha on 26 July) as the fire burned through fine fuels and brush on the steep south-facing slopes of the Merced River canyon. The fire slowed appreciably on 27 July, burning only 271 ha as it crested the canyon rim and expanded through less-steep terrain. On 28 July, the day of our observations, the fire expanded by another 180.5 ha, with most of the growth along a narrow uphill region on the

north flank of the fire (the white arrow in Fig. 1a). The fuels in this region were “heavy,” consisting of deep duff layers and mixed conifers. The total fuel load was estimated to be $7\text{--}10\text{ kg m}^{-2}$ (L. Tarney, National Park Service, 2015, personal communication). Within the expanding fire flank, the fire burned intensely along a narrow swath that was about 200 m wide and 400 m long (the burn-intensity map is available online

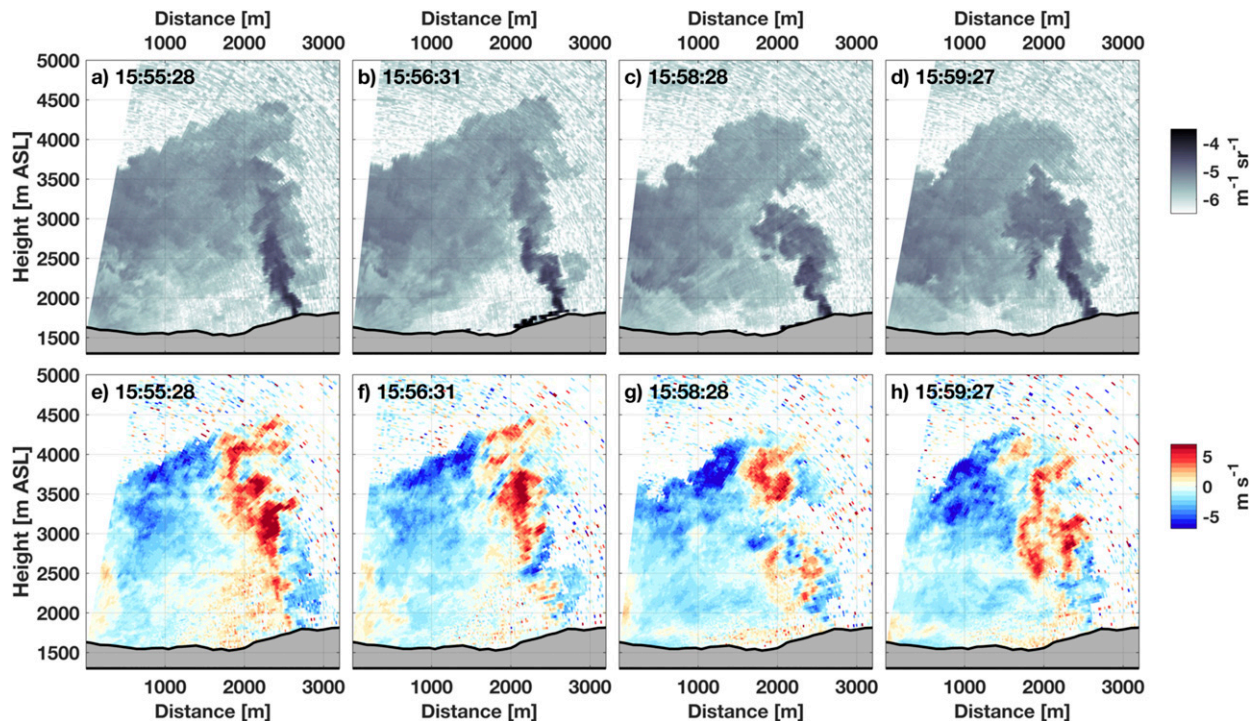


FIG. 2. Lidar RHI scans detailing the plume rise: (a)–(d) smoke backscatter and (e)–(h) radial velocity, where reddish shades indicate flow away from the lidar and bluish shades indicate flow toward the lidar. The time (PDT) is shown for each scan.

at https://www.nps.gov/yose/learn/management/upload/EI-Portal-ES_FINAL.pdf), from which a towering convective plume developed. This plume was the target of our observations.

4. Plume observations

a. Overview

The organized convective column began to form at ~ 1440 Pacific daylight time (PDT). A representative photograph of the plume at 1502 PDT is shown in Fig. 1b, indicating that the smoke-filled convective column possesses many microscale eddies, tilts with the wind aloft, and detrains smoke toward the south (left side of the photograph). As the plume developed, the lidar was scanned along the center of the column, and a total of 116 RHIs were conducted between 1450 and 1630 PDT. The mean scan azimuth was 277° (the white dashed line in Fig. 1a), and minor azimuthal adjustments were made to keep the lidar beam centered on the slowly progressing plume, the base of which traveled about 400 m to the north-northeast during the observing period.

Figure 2 provides four representative lidar RHI scans of the smoke plume, revealing many of the same elements that are apparent in the photograph, albeit at a later time. Figures 2a–d show the lidar backscatter (gray shading),

which is indicative of smoke concentration. The smoke corresponds to values from -6 to $-4 \text{ m}^{-1} \text{ sr}^{-1}$, with lower values indicative of clear air. Figures 2e–h display the corresponding radial velocity data, where red and blue shades are outbound and inbound velocities, respectively. Together these RHI data detail both the overall plume structure and some of the kinematic aspects of microscale mixing therein. Scans of this kind were conducted up until the plume dissipated from decreased fire activity.

b. Ambient environment

Figure 3 shows the ambient potential temperature and wind profile during the plume rise as measured from a radiosonde, the microwave profiler, and surface temperature observations. The radiosonde was launched at 1040 PDT from a position ~ 35 km southwest of the fire. The launch location was chosen to avoid interfering with the operations of fire-suppression aircraft. Despite the distance, the radiosonde data agree well with the microwave profiler observations, which were collected from the truck location adjacent to the fire. The surface potential temperature data (the red dots in Fig. 3a), obtained from weather stations at varying altitudes within 25 km of the fire, provide an estimate of convective boundary layer (CBL) depth. To be specific, the mean potential temperature among these observations is

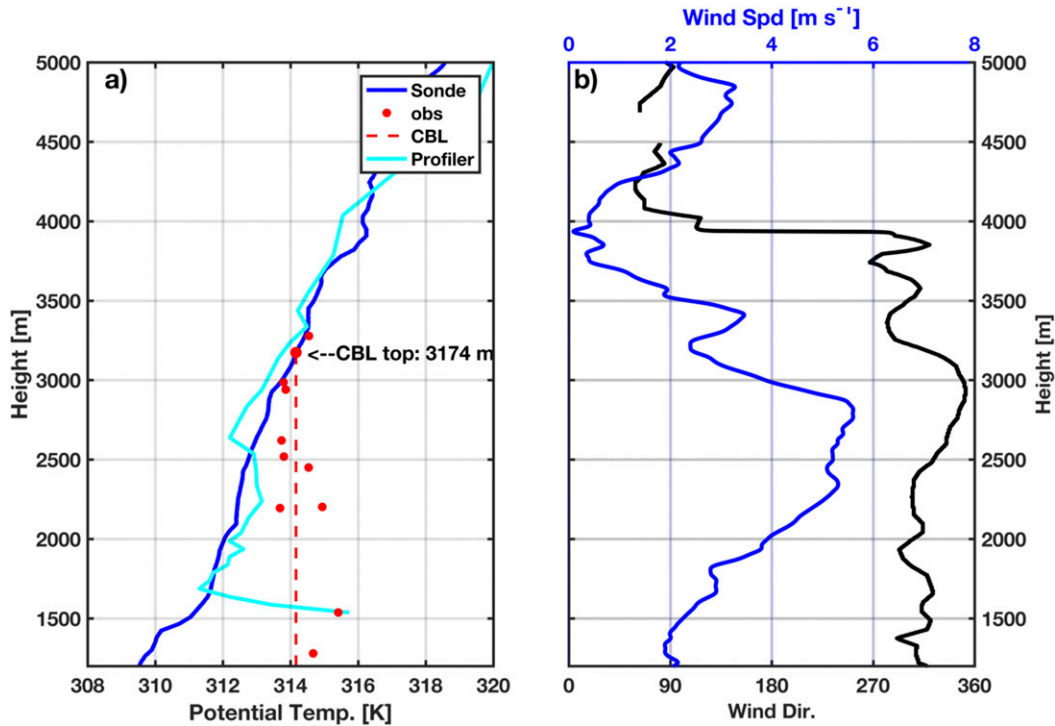


FIG. 3. Atmospheric profiles for 28 Jul 2014. (a) Potential temperature profiles from the 1740 PDT radiosonde (blue line), microwave profiler (cyan line), and surface weather stations (red dots) and the inferred CBL structure (dashed red line). The approximate CBL height is indicated. (b) Wind speed (blue) and direction (black) profiles from the radiosonde.

used to estimate a CBL top of ~ 3174 m above mean sea level (MSL). Above this level, the stratification is roughly constant with height. The mean wind in the CBL, determined from the radiosonde, is 4.2 m s^{-1} from 322° . In the following analyses of the plume rise we use a value of 2.97 m s^{-1} , however, which is the projection of the mean wind onto the mean lidar azimuth angle of 277° .

c. Observed plume structure

1) SMOKE BACKSCATTER

Figure 4a shows the time-mean backscatter computed from all 116 RHI scans between 1450 and 1630 PDT. These data reveal that the time-mean convective column exhibits the form of a bent-over plume in a crosswind (Briggs 1975) that penetrates into the stable layer aloft. The mean smoke detrainment height is near the CBL top (~ 3174 m), and the mean penetration of the plume center above the CBL is ~ 300 m, although it occasionally is as much as 1 km.

The centerline of the time-mean plume is computed by locating the maximum backscatter along each lidar radial (the yellow stars in Fig. 4a). The coordinates of these points are then regressed against the Briggs plume-rise equation for buoyant

plumes in a neutrally stratified environment with a crosswind:

$$z = C \frac{F_0^{1/3}}{U} x^{2/3}, \tag{1}$$

where z is the height of the plume center, U is the mean wind in the CBL (2.97 m s^{-1}), x is the downwind distance (positive to the left), F_0 is the area-integrated buoyancy flux at the plume base, and C is a constant that is defined as

$$C = \left(\frac{2}{3} \beta^2 \right)^{1/3}, \tag{2}$$

with β being an empirical entrainment parameter, which for bent-over plumes is 0.6 (Briggs 1975; Weil 1988; Viegas 1998). The fitted plume-rise centerline from Eq. (1) is superimposed on Fig. 4a as a cyan dashed line and shows good agreement with the lidar observations up to, and even somewhat above, the level of the capping inversion. The Pearson correlation coefficient squared between the fitted centerline and the observed data is $r^2 = 0.98$. An independent curvilinear regression was also conducted, yielding an $x^{0.64}$ relationship, which is close to the two-thirds exponential relationship of Eq. (1).

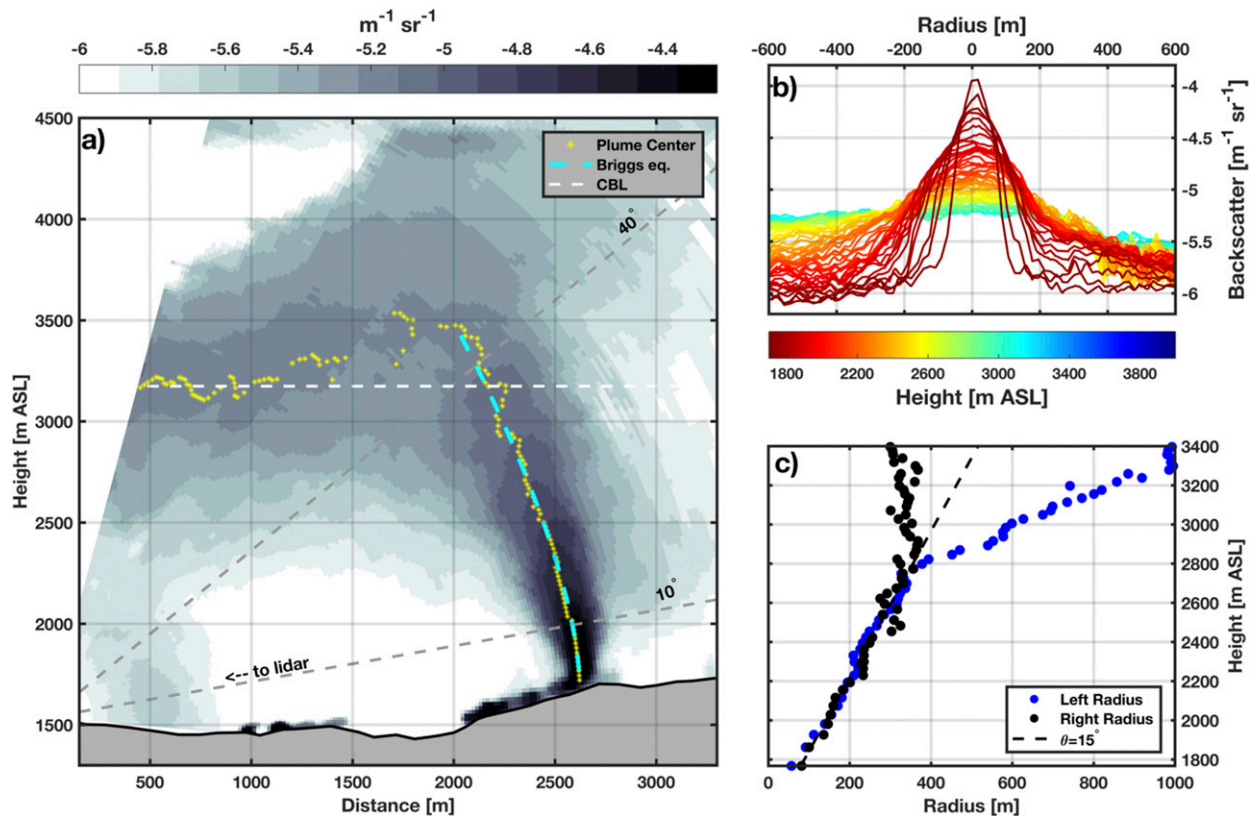


FIG. 4. Overview of the time-mean plume structure. (a) Time-mean backscatter (gray shading), with the plume center points (yellow stars), the plume centerline as given by the Briggs plume-rise equation (dashed cyan line), and the CBL top height (dashed white line). Also shown for reference are lidar radials at elevation angles of 10° and 40° (dashed gray lines) and the direction to the lidar. (b) Backscatter cross sections, taken normal to the plume centerline, as a function of height. The line color indicates the height in the plume, as given by the key. (c) Plume radius as a function of height for the right (black dots) and left (blue dots) plume edge. The right plume edge is considered to be the windward side. Shown for reference is a plume spread angle θ of 15° (dashed line).

Plume cross sections, taken normal to the centerline, reveal a Gaussian distribution of backscatter (and thus smoke), the amplitude of which decays with height (Fig. 4b). Along each cross section, the plume radius is determined using the “half-width at half maximum” amplitude of the backscatter. The maximum amplitude is defined here as the difference between the smoke backscatter at the plume center and the clear-air backscatter ($-6 \text{ m}^{-1} \text{ sr}^{-1}$). The plume edges are thus identified as the first points to the right and left of the plume center that fall below the half-maximum-amplitude threshold. The resulting edge points indicate that the plume radius increases linearly with height from $\sim 100 \text{ m}$ at the plume base to 380 m at 2800 m MSL (Fig. 4c). Above that point, the plume becomes less symmetric. The linear increase in radius, Gaussian cross section, and decrease in smoke concentration with height are all consistent with laboratory and theoretical studies of entraining buoyant plumes (e.g., Morton et al. 1956).

2) ESTIMATED HEAT FLUX

Following the approach of Benech et al. (1988), the observed plume-rise centerline and crosswind are used to invert Eq. (1) to estimate the source buoyancy flux. In so doing we find a mean buoyancy flux F_0 of $8.31 \times 10^4 \text{ m}^4 \text{ s}^{-3}$. Next, using the observed radius at the plume base ($r = 100 \text{ m}$) the time-mean sensible heat flux H_s is determined from

$$H_s = \left(\frac{\pi r^2 g}{\rho_a C_p T_a} \right)^{-1} F_0, \quad (3)$$

where T_a is the ambient temperature (297 K), ρ_a is the ambient air density (1.08 kg m^{-3}), C_p is the specific heat at constant pressure, and πr^2 is the plume cross-sectional area at the base (Viegas 1998). The resulting value of H_s is 86.9 kW m^{-2} , which falls within the reported range of sensible heat fluxes from prescribed fires (from 8 kW m^{-2} to 3 MW m^{-2}), although those fluxes span a

very wide range because of differences in fuels, atmospheric conditions, and fire behavior (Clark et al. 1999; Coen et al. 2004; Clements et al. 2007; Frankman et al. 2013).

3) VELOCITY FIELD

The time-mean radial velocity is shown in Fig. 5, where blue colors indicate radial inbound flow and red colors indicate outbound flow. Inbound, in this context, indicates flow along a radial toward the lidar and is not a plume-relative quantity. Likewise, outbound indicates flow away from the lidar. On the basis of this convention, the plume base is characterized by radial convergence. To be specific, below the 10° elevation radial, inbound flow of 2–3 m s⁻¹ is observed to the right of the plume (blue colors and arrow near point B in Fig. 5), whereas the flow to the left of the plume base is weakly outbound in a region that extends more than 1 km toward the lidar (reddish shading and arrow near point A in Fig. 5). This portion of the flow is evidence of a fire-induced perturbation of the ambient wind field that extends 1 km from the plume base. From these mean radial velocity data, the radial component of the convergence is estimated to be ~ 0.05 s⁻¹.

Aloft, regions of both convective overshoot and sinking flow are observed (points C and D, respectively, in Fig. 5). For example, at point C large outbound radial velocities are associated with regions of smoke residing above the mean detrainment level. In contrast, at point D a coherent region of inbound velocities coincides with smoke subsiding toward its detrainment level near the CBL top (i.e., 3174 m). In both locations, the observed radial velocities are the projection of the horizontal and vertical flows in the upper plume onto the lidar radial.

The convergence at the plume base is linked to the fire-induced updraft. The updraft itself is not directly measured by the lidar but can be estimated by tracking the position of convective elements with time as they ascend through the plume. For example, in Fig. 6 the leading edge of a convective element, denoted with a magenta circle, is traced through a sequence of four RHI scans. From these positions, the ascent rate for the convective element is estimated to be 13.5, 10.7, and 7.6 m s⁻¹, indicating a vigorous updraft that decays with height. The convective element (i.e., a “puff”) is also observed to expand in scale as it ascends through the plume.

4) TURBULENT PLUME STRUCTURE

The time-varying structure of the plume is examined in Fig. 7. Shown are the backscatter variance (Fig. 7a),

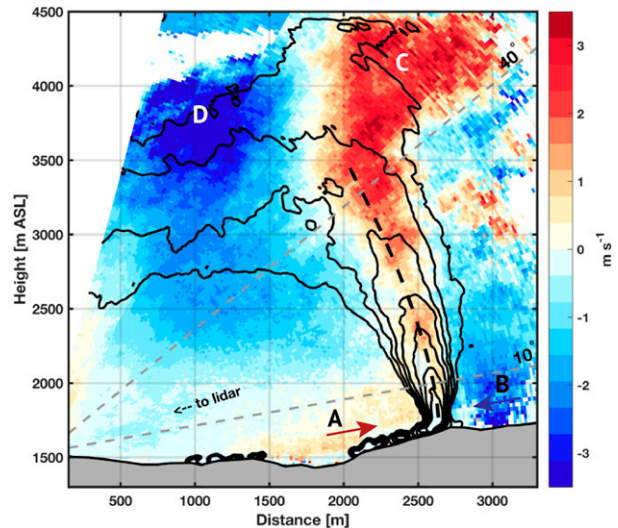


FIG. 5. Time-mean radial velocity (color shading) with the mean smoke backscatter (black contours, with a contour interval of 0.25 m⁻¹ sr⁻¹) and the plume centerline (black dashed line). Reddish shades indicate flow away from the lidar, and bluish shades indicate flow toward the lidar. The 10° and 40° elevation-angle radials are shown for reference, and the direction to the lidar is indicated. Points A, B, C, and D are discussed in the text. The arrows near A and B indicate the radial flow direction.

radial velocity variance (Fig. 7b), and temporal covariance of the backscatter and radial velocity (Fig. 7c).

The backscatter variance results from changes in smoke concentration associated with turbulent eddies and variations in the smoke emissions. The highest variability in smoke concentration occurs along the flanks of the plume where the gradient in backscatter is largest. The low variance along the plume centerline suggests that the source variability in smoke emissions is relatively small in comparison with the mixing due to eddies along the plume edges. These data also indicate that the plume core remains somewhat (although not completely) protected from entrainment at each height, which is consistent with the Gaussian cross sections shown in Fig. 4b.

When compared with the smoke variance, the radial velocity variance is less symmetric about the plume centerline (Fig. 7b). To be specific, the radial velocity variance is largest along the right edge of the plume where the strongest individual convective elements rise (i.e., the stronger the buoyancy is the more upright is the plume; Viegas 1998). The maximum variance values along the right plume edge range from 7 to 14 m² s⁻² (2.6–3.7 m s⁻¹ standard deviation).

The temporal covariance between the smoke backscatter and the radial velocity for the entire observing period is presented in Fig. 7c. Although these data do

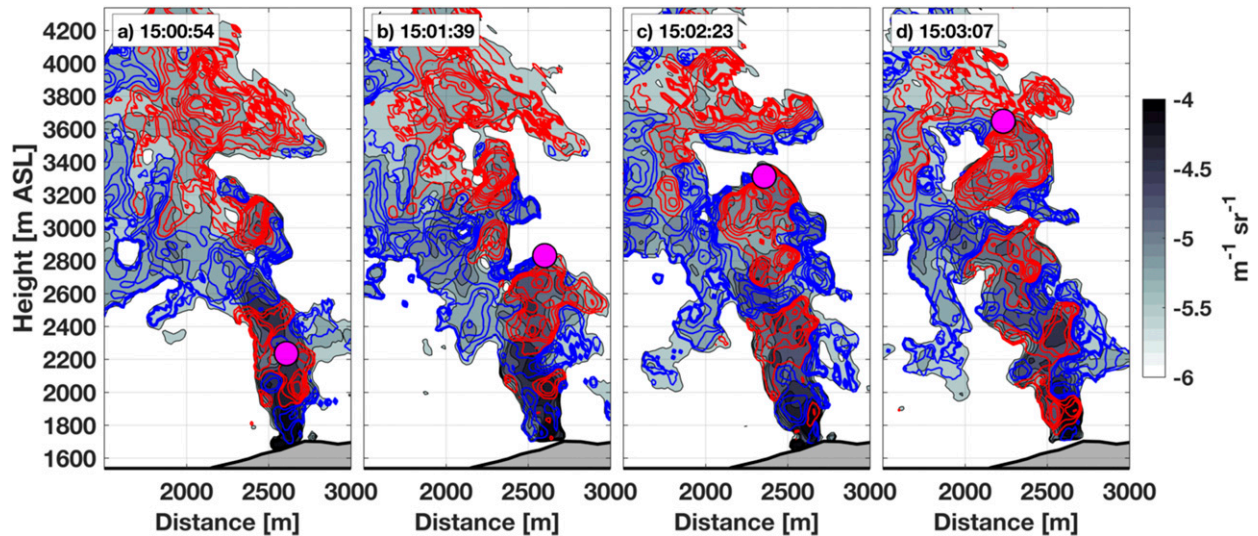


FIG. 6. Sequence of times (PDT) showing the rise of an isolated convective element through the plume. The backscatter is shown as gray shading. The inbound radial velocity is indicated as blue contours, and the outbound velocity is shown by red contours (the contour interval is 1 m s^{-1}). The top of a single convective element tracked through the plume is indicated with a magenta circle.

not have physical units ($\text{s}^{-2} \text{sr}^{-2}$), they are nonetheless very informative. Of note is that the covariance changes sign across the plume centerline. Along the far edge of the plume, positive radial velocity perturbations (i.e., enhanced outbound flow) correspond to positive smoke backscatter perturbations and, therefore, positive covariance. The opposite is true on the near edge of the plume, yielding negative covariance. These data

indicate that coherent smoke–velocity fluctuations redistribute smoke outward from the plume core and mix clear air inward. The covariance thus shows a portion of the entrainment processes contributing to plume dilution with height, which affects the plume rise and smoke dispersion.

Figures 8a–c show selected RHI scans that are demonstrative of the entrainment dynamics described

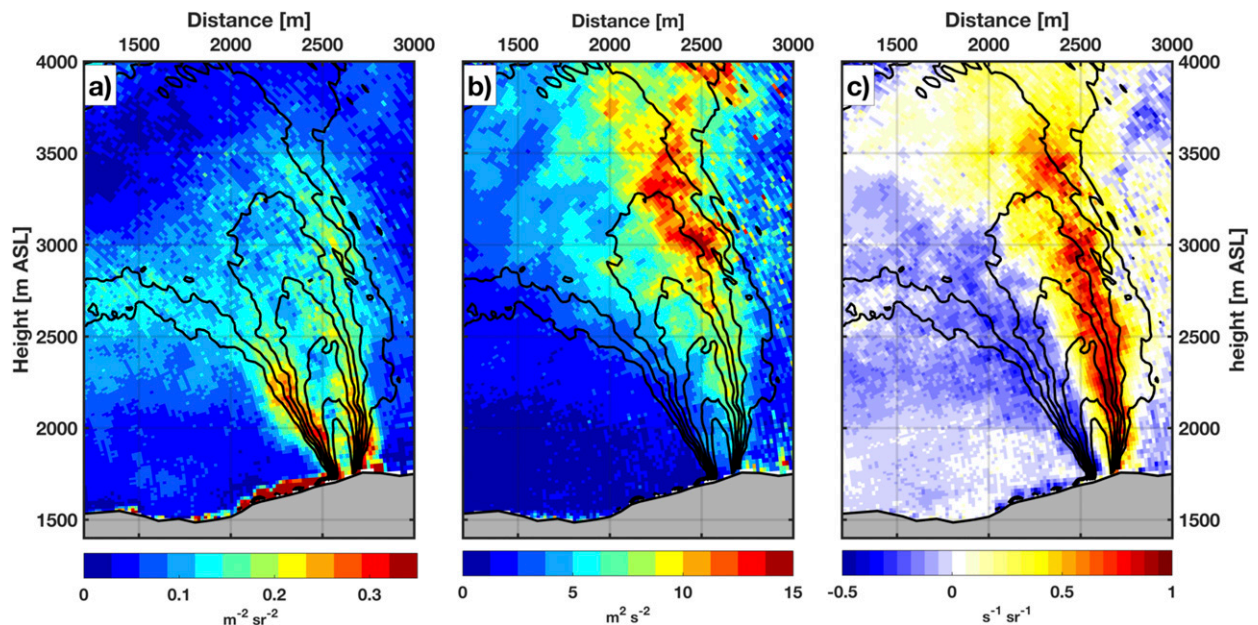


FIG. 7. Turbulent variations in the plume structure: (a) variance of the smoke backscatter, (b) variance of the radial velocity, and (c) covariance of the smoke backscatter and radial velocity. The mean backscatter is also shown (black contours, with a contour interval of $0.25 \text{ m}^{-1} \text{ sr}^{-1}$).

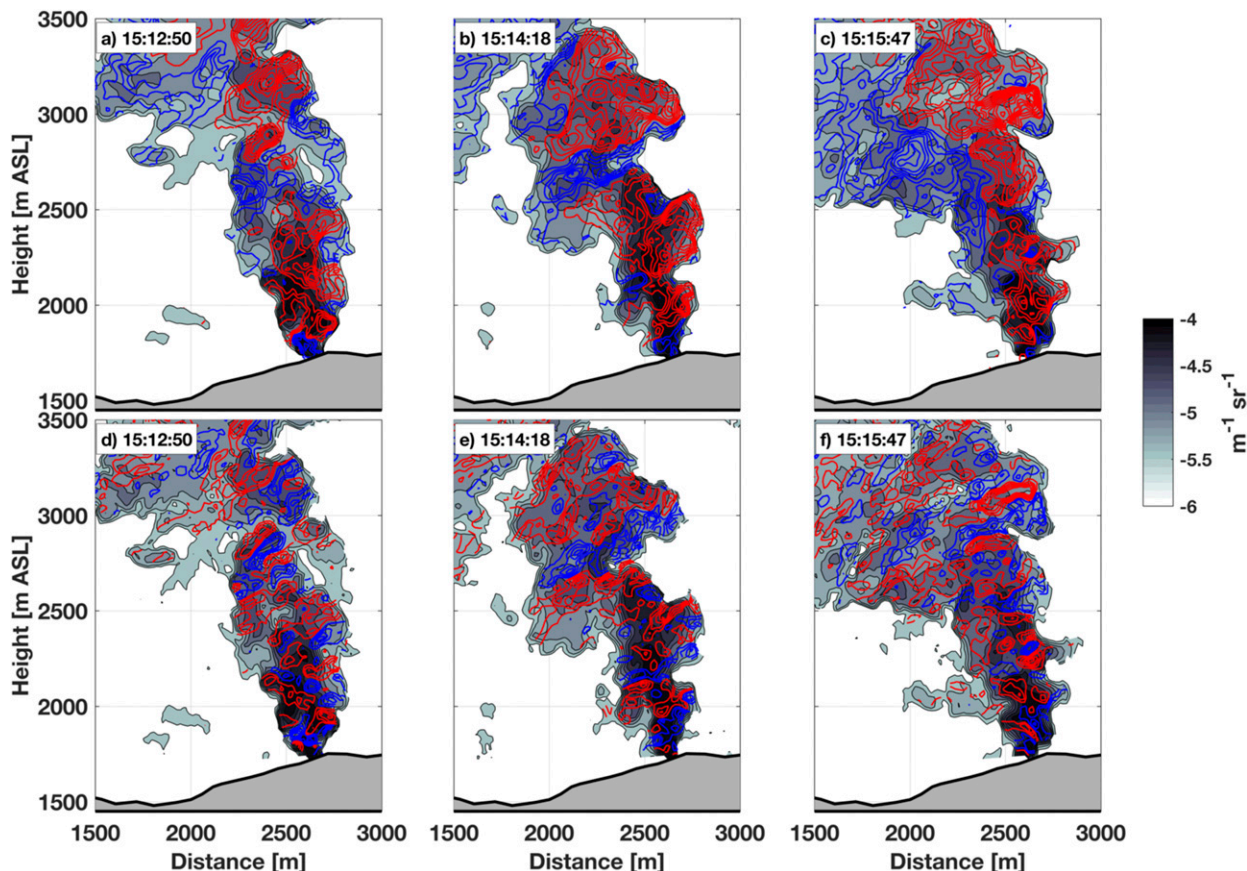


FIG. 8. Smoke, velocity, and shear variations during select RHI scans at three different times (PDT) for smoke backscatter (gray shading) and (a)–(c) radial velocity (red and blue contours, with a contour interval of 1 m s^{-1}) or (d)–(f) radial shear (red and blue contours, with a contour interval of 0.04 s^{-1}).

above. From these examples, it is apparent that along the right edge of the plume the outward protrusions of smoke tend to correspond with increased outbound flow (red contours). Likewise, on the left side of the plume smoke protrusions correspond to increased inbound flow (blue contours). These data also show that significant wind shear characterizes the eddies that contribute to entrainment (Figs. 8d–f). Here shear is measured as the change in radial velocity between adjacent elevation steps. The shear of the radial velocity is organized in quasi-regular alternating regions of positive and negative shear that are spaced $\sim 100 \text{ m}$ apart. Visual observations suggest that these regions of shear are associated with vortices that are prevalent along the plume edges and are a key mechanism in entrainment (see the arrow in Fig. 1b).

5. Summary and conclusions

In this study, Doppler lidar observations of the mean and turbulent structure of a wildfire convective plume were examined. The mean plume exhibited the expected

form of a bent-over plume in a crosswind and penetrated to a substantial depth ($\sim 1 \text{ km}$) in a capping inversion layer aloft. The Briggs plume-rise equation was fitted to these observed plume data and then inverted to estimate a fire-induced heat flux of 87 kW m^{-2} . The plume was also found to have a linearly increasing radius with height and a Gaussian cross section in smoke concentration (i.e., lidar backscatter), consistent with classical plume-rise assumptions. Taken together, these findings demonstrate that high-spatiotemporal-resolution measurements of the plume rise can be used to estimate fire intensity.

This study also provided some insight into entrainment structures in a wildfire convective plume. The lidar data revealed the prevalence of $O(100 \text{ m})$ -scale eddies within the plume that contribute to the covariance of smoke backscatter and radial velocity perturbations. The sign of the covariance is such that smoke is distributed outward and clear air is distributed inward, thus diluting the smoke concentration and increasing the plume radius with height via entrainment.

The results of this single case study indicate that the well-known Briggs plume-rise equation provides a good description of the observed plume structure, but some caveats must be addressed. On the day of our observations, the El Portal fire was slowly evolving and the plume developed from an isolated expanding flank of the fire. The plume also grew into a neutrally stratified boundary layer capped with an inversion layer. Combined, these factors make the application of the Briggs equation relatively straightforward. More-complex fire perimeters, multicore updrafts, and plume interaction with complex stratification or wind shear would all strain the applicability of the Briggs plume-rise equation. In such cases, more-sophisticated plume-rise models are likely necessary to predict smoke injection heights. To this end, future investigations of this kind should link high-spatiotemporal-resolution observations of fire intensity, atmospheric structure, and plume-rise dynamics to understand better the processes affecting smoke injection height from wildfires.

Acknowledgments. The authors thank Yosemite National Park (YNP) for the research permit (YOSE-2012-SCI-0109) and permission to make measurements during the El Portal fire. In addition, we thank Dr. Leland Tarney and Joe Meyer from YNP for providing GIS data and fuel-loading estimates. The authors also thank Braniff Davis and Richard Bagley for help in the field during the deployment. In addition, we acknowledge the Tahoe National Forest for managing our fire-line qualifications. This research was supported by funding from the National Science Foundation (AGS-1151930).

REFERENCES

- Achtemeier, G. L., S. A. Goodrick, Y. Liu, F. Garcia-Menendez, Y. Hu, and M. T. Odman, 2011: Modeling smoke plume-rise and dispersion from southern United States prescribed burns with Daysmoke. *Atmosphere*, **2**, 358–388, doi:10.3390/atmos2030358.
- Andreae, M. O., D. Rosenfeld, P. Artaxo, A. A. Costa, G. P. Frank, K. M. Longo, and M. A. F. Silva-Dias, 2004: Smoking rain clouds over the Amazon. *Science*, **303**, 1337–1342, doi:10.1126/science.1092779.
- Ashley, W. S., S. Strader, D. C. Dziubla, and A. Haberlie, 2015: Driving blind: Weather-related vision hazards and fatal motor vehicle crashes. *Bull. Amer. Meteor. Soc.*, **96**, 755–778, doi:10.1175/BAMS-D-14-00026.1.
- Banta, R. M., L. D. Olivier, E. T. Holloway, R. A. Kropfli, B. W. Bartram, R. E. Cupp, and M. J. Post, 1992: Smoke-column observations from two forest fires using Doppler lidar and Doppler radar. *J. Appl. Meteor.*, **31**, 1328–1349, doi:10.1175/1520-0450(1992)031<1328:SCOFTF>2.0.CO;2.
- Benech, B., 1976: Experimental study of an artificial convective plume initiated from the ground. *J. Appl. Meteor.*, **15**, 127–137, doi:10.1175/1520-0450(1976)015<0127:ESOAAC>2.0.CO;2.
- , P. Van Dinh, A. Ezcurra, and J. L. Lesne, 1988: Investigation of a 1000-MW smoke plume by means of a 1.064 μm lidar—II. Determination of diffusion characteristics of the plume particles. *Atmos. Environ.*, **22**, 1071–1084, doi:10.1016/0004-6981(88)90337-X.
- Briggs, G. A., 1975: Plume rise predictions. *Lectures on Air Pollution and Environmental Impact Analyses*, D. A. Haugen, Ed., Amer. Meteor. Soc., 59–111.
- Charland, A. M., and C. B. Clements, 2013: Kinematic structure of a wildland fire plume observed by Doppler lidar. *J. Geophys. Res. Atmos.*, **118**, 3200–3212, doi:10.1002/jgrd.50308.
- Church, C. R., J. T. Snow, and J. Dessens, 1980: Intense atmospheric vortices associated with a 1000 MW fire. *Bull. Amer. Meteor. Soc.*, **61**, 682–694, doi:10.1175/1520-0477(1980)061<0682:IAVAWA>2.0.CO;2.
- Clark, T. L., L. Radke, J. Coen, and D. Middleton, 1999: Analysis of small-scale convective dynamics in a crown fire using infrared video camera imagery. *J. Appl. Meteor.*, **38**, 1401–1420, doi:10.1175/1520-0450(1999)038<1401:AOSSCD>2.0.CO;2.
- Clements, C. B., and A. J. Oliphant, 2014: The California State University Mobile Atmospheric Profiling System: A facility for research and education in boundary layer meteorology. *Bull. Amer. Meteor. Soc.*, **95**, 1713–1724, doi:10.1175/BAMS-D-13-00179.1.
- , S. Zhong, S. Goodrick, J. P. Li, X. Bian, W. E. Heilman, and M. Patel, 2007: Observing the dynamics of wildland grass fires: FireFlux—a field validation experiment. *Bull. Amer. Meteor. Soc.*, **88**, 1369–1382, doi:10.1175/BAMS-88-9-1369.
- , and Coauthors, 2016: Fire weather conditions and fire-atmosphere interactions observed during low-intensity prescribed fires—RxCADRE 2012. *Int. J. Wildland Fire*, **25**, 90–101, doi:10.1071/WF14173.
- Coen, J., S. Mahalingam, and J. Daily, 2004: Infrared imagery of crown-fire dynamics during FROSTFIRE. *J. Appl. Meteor.*, **43**, 1241–1259, doi:10.1175/1520-0450(2004)043<1241:IIOCDD>2.0.CO;2.
- Cunningham, P., and S. L. Goodrick, 2013: High-resolution numerical models for smoke transport in plumes from wildland fires. *Remote Sensing and Modeling Applications to Wildland Fires*, J. J. Qu et al., Eds., Springer, 67–79.
- Delfino, R. J., and Coauthors, 2009: The relationship between respiratory and cardiovascular hospital admissions to the southern California wildfires of 2003. *Occup. Environ. Med.*, **66**, 189–197, doi:10.1136/oem.2008.041376.
- Frankman, D., B. W. Webb, B. W. Butler, D. Jimenez, J. M. Forthofer, P. Sopko, and R. D. Ottmar, 2013: Measurements of convective and radiative heating in wildland fires. *Int. J. Wildland Fire*, **22**, 157–167, doi:10.1071/WF11097.
- Freitas, S. R., K. M. Longo, and M. O. Andreae, 2006: Impact of including the plume rise of vegetation fires in numerical simulations of associated atmospheric pollutants. *Geophys. Res. Lett.*, **33**, L17808, doi:10.1029/2006GL026608.
- , and Coauthors, 2007: Including the sub-grid scale plume rise of vegetation fires in low resolution atmospheric transport models. *Atmos. Chem. Phys.*, **7**, 3385–3398, doi:10.5194/acp-7-3385-2007.
- , K. Longo, J. Trentmann, and D. Latham, 2010: Technical note: Sensitivity of 1-D smoke plume rise models to the inclusion of environmental wind drag. *Atmos. Chem. Phys.*, **10**, 585–594, doi:10.5194/acp-10-585-2010.
- Fromm, M., D. T. Lindsey, R. Servranckx, G. Yue, T. Trickl, R. Sica, and S. Godin-Beekmann, 2010: The untold story of

- pyrocumulonimbus. *Bull. Amer. Meteor. Soc.*, **91**, 1193–1209, doi:10.1175/2010BAMS3004.1.
- Hiscox, A. L., C. J. Nappo, and D. R. Miller, 2006: On the use of lidar images of smoke plumes to measure dispersion parameters in the stable boundary layer. *J. Atmos. Oceanic Technol.*, **23**, 1150–1154, doi:10.1175/JTECH1896.1.
- Holstius, D. M., C. E. Rei, B. M. Jesdale, and R. Morello-Frosch, 2012: Birth weight following pregnancy during the 2003 Southern California wildfires. *Environ. Health Perspect.*, **120**, 1340–1345, doi:10.1289/ehp.1104515.
- Horel, J., and Coauthors, 2002: MesoWest: Cooperative mesonets in the western United States. *Bull. Amer. Meteor. Soc.*, **83**, 211–225, doi:10.1175/1520-0477(2002)083<0211:MCMITW>2.3.CO;2.
- Johnston, F. H., and Coauthors, 2012: Estimated global mortality attributable to smoke from landscape fires. *Environ. Health Perspect.*, **120**, 695–701, doi:10.1289/ehp.1104422.
- Kahn, R. A., Y. Chen, D. L. Nelson, F.-Y. Leung, Q. Li, D. J. Diner, and J. A. Logan, 2008: Wildfire smoke injection heights: Two perspectives from space. *Geophys. Res. Lett.*, **35**, L04809, doi:10.1029/2007GL032165.
- Kovalev, V. S., J. Newton, C. Wold, and W. M. Hao, 2005: Simple algorithm to determine the near-edge smoke boundaries with scanning lidar. *Appl. Opt.*, **44**, 1761–1768, doi:10.1364/AO.44.001761.
- Lareau, N. P., and C. B. Clements, 2015: Cold smoke: Smoke-induced density currents cause unexpected smoke transport near large wildfires. *Atmos. Chem. Phys.*, **15**, 11 513–11 520, doi:10.5194/acp-15-11513-2015.
- , and —, 2016: Environmental controls on pyrocumulus and pyrocumulonimbus initiation and development. *Atmos. Chem. Phys.*, **16**, 4005–4022, doi:10.5194/acp-16-4005-2016.
- Linden, P. F., 1973: The interaction of a vortex ring with a sharp density interface. *J. Fluid Mech.*, **60**, 467–480, doi:10.1017/S0022112073000303.
- Luderer, G., J. Trentmann, T. Winterrath, C. Textor, M. Herzog, H. F. Graf, and M. O. Andreae, 2006: Modeling of biomass smoke injection into the lower stratosphere by a large forest fire (Part II): Sensitivity studies. *Atmos. Chem. Phys.*, **6**, 5261–5277, doi:10.5194/acp-6-5261-2006.
- , —, and M. O. Andreae, 2009: A new look at the role of fire-released moisture on the dynamics of atmospheric pyro-convection. *Int. J. Wildland Fire*, **18**, 554–562, doi:10.1071/WF07035.
- Manins, P. C., 1979: Partial penetration of an elevated inversion layer by chimney plumes. *Atmos. Environ.*, **13**, 733–741, doi:10.1016/0004-6981(79)90203-8.
- Morton, B. R., G. I. Taylor, and J. S. Turner, 1956: Turbulent gravitational convection from maintained and instantaneous sources. *Proc. Roy. Soc. London*, **234A**, 1–23, doi:10.1098/rspa.1956.0011.
- Pearson, G., F. Davies, and C. Collier, 2009: An analysis of the performance of the UFAM pulsed Doppler lidar for observing the boundary layer. *J. Atmos. Oceanic Technol.*, **26**, 240–250, doi:10.1175/2008JTECHA1128.1.
- Penner, J. E., R. E. Dickinson, and C. S. O'Neill, 1992: Effects of aerosol from biomass burning on the global radiation budget. *Science*, **256**, 1432–1434, doi:10.1126/science.256.5062.1432.
- Radke, L. F., J. H. Lyons, P. V. Hobbs, D. A. Hegg, D. V. Sandberg, and D. E. Ward, 1990: Airborne monitoring and smoke characterization of prescribed fires on forest lands in western Washington and Oregon. U.S. Dept. of Agriculture Forest Service Tech. Rep. PNW-GTR-251, 81 pp. [Available online at https://www.fs.fed.us/pnw/pubs/pnw_gtr251.pdf.]
- , and Coauthors, 1991: Particulate and trace gas emissions from large biomass fires in North America. *Global Biomass Burning: Atmospheric, Climatic and Biospheric Implications*, J. S. Levine, Ed., MIT Press, 209–224.
- Raffuse, S. M., K. J. Craig, N. K. Larkin, T. T. Strand, D. Coe Sullivan, N. J. M. Wheeler, and R. Solomon, 2012: An evaluation of modeled plume injection height with satellite-derived observed plume height. *Atmosphere*, **3**, 103–123, doi:10.3390/atmos3010103.
- Reid, J. S., and P. V. Hobbs, 1998: Physical and optical properties of young smoke from individual biomass fires in Brazil. *J. Geophys. Res.*, **103**, 32 013–32 030, doi:10.1029/98JD00159.
- , R. Koppmann, T. F. Eck, and D. P. Eleuterio, 2005: A review of biomass burning emissions part II: Intensive physical properties of biomass burning particles. *Atmos. Chem. Phys.*, **5**, 799–825, doi:10.5194/acp-5-799-2005.
- Richards, J. M., 1961: Experiments on the penetration of an interface by buoyant thermals. *J. Fluid Mech.*, **11**, 369–384, doi:10.1017/S0022112061000585.
- , 1963: The penetration of interfaces by cylindrical thermals. *Quart. J. Roy. Meteor. Soc.*, **89**, 254–264, doi:10.1002/qj.49708938006.
- Robock, A., 1988: Enhancement of surface cooling due to forest fire smoke. *Science*, **242**, 911–913, doi:10.1126/science.242.4880.911.
- , 1991: Surface cooling due to forest fire smoke. *J. Geophys. Res.*, **96**, 20 869–20 878, doi:10.1029/91JD02043.
- Saunders, P. M., 1962: Penetrative convection in stably stratified fluids. *Tellus*, **14**, 177–194, doi:10.3402/tellusa.v14i2.9539.
- Scorer, R. S., 1957: Experiments on convection of isolated masses of buoyant fluid. *J. Fluid Mech.*, **2**, 583–594, doi:10.1017/S0022112057000397.
- Trentmann, J., and Coauthors, 2006: Modeling of biomass smoke injection into the lower stratosphere by a large forest fire (Part I): Reference simulation. *Atmos. Chem. Phys.*, **6**, 5247–5260, doi:10.5194/acp-6-5247-2006.
- Val Martin, M., J. A. Logan, R. A. Kahn, F. Y. Leung, D. L. Nelson, and D. J. Diner, 2010: Smoke injection heights from fires in North America: Analysis of 5 years of satellite observations. *Atmos. Chem. Phys.*, **10**, 1491–1510, doi:10.5194/acp-10-1491-2010.
- , R. Kahn, J. A. Logan, R. Paugam, M. Wooster, and C. M. Ichoku, 2012: Space-based observational constraints for 1-D fire smoke plume-rise models. *J. Geophys. Res.*, **117**, D22204, doi:10.1029/2012JD018370.
- Viegas, D. X., 1998: Convective processes in forest fires. *Buoyant Convection in Geophysical Flows*, E. J. Plate et al., Eds., Springer, 401–420.
- Wegesser, T. C., K. E. Pinkerton, and J. A. Last, 2009: California wildfires of 2008: Coarse and fine particulate matter toxicity. *Environ. Health Perspect.*, **117**, 893–897, doi:10.1289/ehp.0800166.
- Weil, J. C., 1988: Plume rise. *Lectures on Air Pollution Modeling*, A. Venkatram, Ed., Amer. Meteor. Soc., 119–166.